19

Maximizing Local Access to Therapeutic Deliveries in Glioblastoma. Part III: Irreversible Electroporation and High-Frequency Irreversible Electroporation for the Eradication of Glioblastoma

MELVIN F. LORENZO[1] • CHRISTOPHER B. ARENA[1,2] • RAFAEL V. DAVALOS[1]

[1]School of Biomedical Engineering and Sciences, Virginia Tech-Wake Forest University, Blacksburg, VA, USA; [2]Laboratory for Therapeutic Directed Energy, Department of Physics, Elon University, Elon, NC, USA

Author for correspondence: Rafael V. Davalos, School of Biomedical Engineering and Sciences, Virginia Tech-Wake Forest University, 325 Kelly Hall, Stanger Street, Blacksburg, VA 24061, USA. E-mail: davalos@vt.edu

Doi: http://dx.doi.org/10.15586/codon.glioblastoma.2017.ch19

Abstract: Glioblastoma (GBM) is the most common and aggressive primary brain tumor in adults. Approximately 9180 primary GBM tumors are diagnosed in the United States each year, in which median survival is up to 16 months. GBM eludes and resists typical cancer treatments due to the presence of infiltrative cells beyond the solid tumor margin, heterogeneity within the tumor microenvironment, and protection from the blood–brain barrier. Conventional treatments for GBM, such as surgical resection, radiotherapy, and chemotherapy, have shown limited efficacy;

In: *Glioblastoma*. Steven De Vleeschouwer (Editor), Codon Publications, Brisbane, Australia
ISBN: 978-0-9944381-2-6; Doi: http://dx.doi.org/10.15586/codon.glioblastoma.2017

therefore, alternate treatments are needed. Tumor chemoresistance and its proximity to critical structures make GBM a prime theoretical candidate for nonthermal ablation with irreversible electroporation (IRE) and high-frequency IRE (H-FIRE). IRE and H-FIRE are treatment modalities that utilize pulsed electric fields to permeabilize the cell membrane. Once the electric field magnitude exceeds a tissue-specific lethal threshold, cell death occurs. Benefits of IRE and H-FIRE therapy include, but are not limited to, the elimination of cytotoxic effects, sharp delineation from treated tissue and spared tissue, a nonthermal mechanism of ablation, and sparing of nerves and major blood vessels. Preclinical studies have confirmed the safety and efficacy of IRE and H-FIRE within their experimental scope. In this chapter, studies will be collected and information extrapolated to provide possible treatment regimens for use in high-grade gliomas, specifically in GBM.

Keywords: Blood–brain barrier disruption; Glioblastoma; High-frequency irreversible electroporation; Irreversible electroporation; Treatment planning

Introduction

Glioblastoma (GBM) is the most recurrent, aggressive brain tumor representing ~50% of all primary brain gliomas. Ninety percent of GBM tumors are diagnosed *de novo* as primary tumors, and 10% are diagnosed as secondary tumors, where primary tumors correlate to lower survival rates (1). Approximately 9180 primary GBM tumors are diagnosed in the United States each year, in which median survival is up to 16 months. Current standard of care for malignant gliomas (MGs) include, if feasible, tumor resection followed by radiotherapy (RT) and chemotherapy (CT). Difficulties in treatment of GBM are due to infiltrative cells beyond the solid tumor margin, heterogeneity within tumor microenvironment, and protection from the blood–brain barrier (BBB) (1). Due to dismal prognosis of patients with GBM, quality of life (QoF) post-treatment is an important factor when considering treatment options. Aside from temozolomide (TMZ), cytotoxic chemotherapeutic agents do not significantly alter prognosis outcomes (2). Therefore, new aims in therapy for MGs include reducing morbidity, maintaining and improving QoF, and preserving neurologic function.

Recent advancements in the treatment of GBM have marginally extended median survival rates. These improvements seem to be dependent on GBM cellular morphology rather than improvement of holistic treatment regimes. In a study conducted by Glas et al., the overall 5-year survival rate in a cohort of 39 patients was reported to be 15.8%, which is much higher than the usually reported rate between 4 and 5% (3). This study utilized a combination of tumor resection and RT, followed by delivery of CT agents, lomustine (CCNU) and TMZ. Significant findings include increased dosage of CCNU and TMZ resulted in greater survival rates with comparable toxicities among standard doses, as well as a link between long-term survival and the O-methylguanine-DNA methyltransferase (MGMT) gene (3). Nonetheless, GBM remains a lethal and aggressive tumor that evades standard treatment; therefore, alternative approaches are discussed.

Irreversible Electroporation and High-Frequency Irreversible Electroporation for the Eradication of GBM

REVERSIBLE ELECTROPORATION

The cell membrane acts as a selectively permeable barrier that regulates the transport of ions and molecules. It is composed of a phospholipid bilayer and protein channels that together maintain homeostasis. Therapies dependent on the transport of molecules across the membrane rely heavily on cell permeabilization without causing damage to the cell, which can be achieved, for example, with focused ultrasound (4–6). In this chapter, we present the use of electroporation as a means of accomplishing cell permeabilization. Electroporation is a phenomenon in which the cell membrane undergoes a physiological transformation caused by pulsed electric fields (PEFs). Following the application of PEFs, naturally occurring hydrophobic pores, or defects, in the membrane transition to lipid-lined hydrophilic pores through which polar molecules can pass (7). This transition occurs as an energy minimization with pore radius, and increasing the transmembrane potential (TMP) by applying PEFs further decreases pore energy and increases hydrophilic pore creation rate. Once created, the hydrophilic pores can expand or reseal depending on the pulse parameters. The net effect of PEFs on tissue is transient permeabilization of the phospholipid bilayers of individual cells, as well as heat generation. Generally, a TMP of ~0.5 V is needed to induce reversible electroporation (RE), a process marked by rapid depolarization of the cell membrane and delayed resealing of transient, nanoscale defects (8, 9). Figure 1 depicts pore formation using molecular dynamics simulations after 50 ns as performed by Böchman et al. (10).

During RE, the cell membrane exhibits a tremendous increase in molecular transport. This phenomenon has been exploited in electrochemotherapy (ECT) to improve cellular uptake of cytotoxic drugs, such as bleomycin or cisplatin, and increase drug cytotoxicity (11). It has also been used to deliver genetic material, plasmid DNA, into cells to correct genetic disorders, in a process known as DNA electrotransfer or electrogene therapy (12).

Clinically, RE is administered through two or more electrodes placed into or around the target tissue, as depicted in Figure 2A. Using custom electrodes, Gehl et al. inoculated mice with N32 glioma-derived cells and treated them with ECT using bleomycin as the chemotherapeutic agent. Nine of 13 mice showed tumor regression and elimination, while 4 mice showed tumor progression. Of the four mice that showed tumor progression, three mice were identified to have the largest tumor volumes of the study. Lack of eradication was attributed to incomplete electroporation and envelopment of the tumor within electric field thresholds needed to induce RE and increase cytotoxicity (13). ECT has also been used in the treatment of metastases from melanoma, breast, and head and neck cancer (14). Recently, Gehl et al. performed ECT using calcium as a substitute for cytotoxic drugs. This process, known as calcium electroporation, demonstrated its ability to induce ATP depletion-associated cellular death with NaCl and $CaCl_2$ (15, 16).

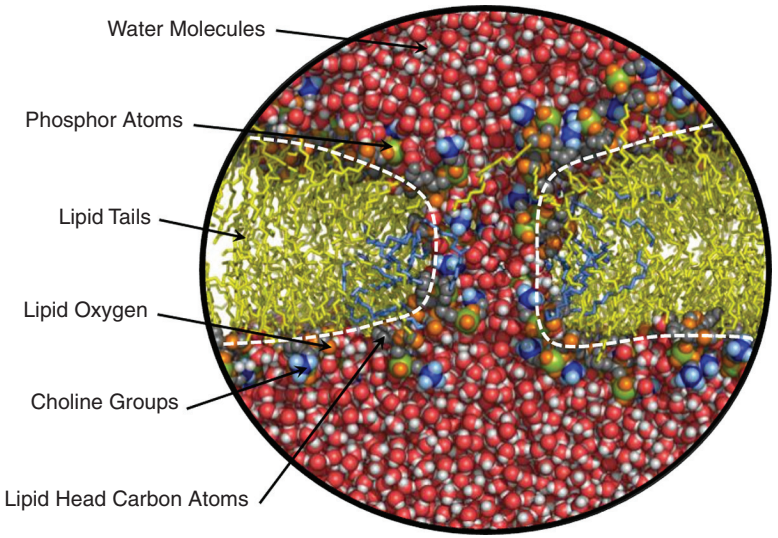

Figure 1 Pore formation as modeled by Böckmann et al. Molecular dynamics simulation of pore formation after 50 ns shown as a section through the lipid bilayer membrane. The outline of the hydrophilic pore is shown by the white dashed lines. The pore starts off in an impermeable hydrophobic state, transitions into a hydrophobic pore intermediate, and finishes off as a stable hydrophilic pore. (Adapted from Biophys J 2008;95(4):1837–1850.)

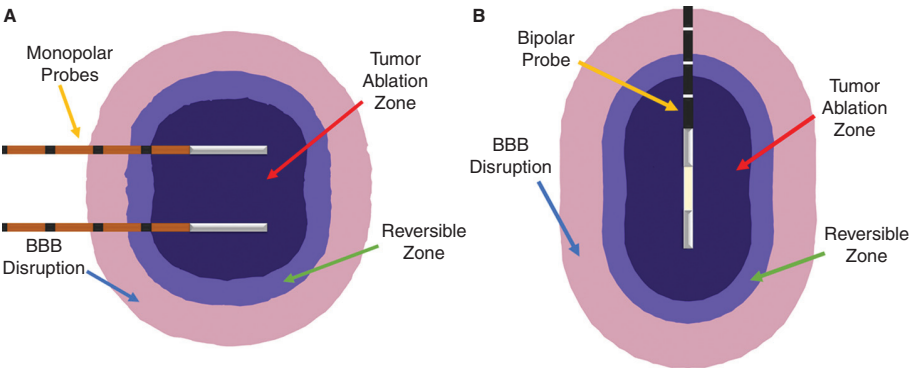

Figure 2 Monopolar probe and bipolar probe insertion. Clinical application of electroporation is achieved by inserting either (**A**) two monopolar probes or (**B**) a single bipolar probe. One electrode is set to ground while the other is energized and pulsed to produce PEFs. Three zones of interest include the ablation zone, the RE (reversible) zone, as well as the BBB disruption zone. It is debatable whether the BBB disruption zone and the RE zone are separate regions; for illustrative purposes they are modeled individually.

IRREVERSIBLE ELECTROPORATION

More recently, IRE has been developed to directly ablate unwanted tissue by further increasing the TMP through higher electric field magnitudes or by applying additional sets of pulses to prolong pore lifetime. Davalos et al. demonstrated that electric pulses could be applied to raise the TMP past a threshold associated with permanent cell damage, without causing significant thermal damage (17). It is considered that IRE effects occur when the TMP reaches ~1.0V (18). On a cellular level, this increase in TMP also induces nanoscale defects on the cell membrane, resulting in irrevocable disruption in homeostasis ultimately leading to cell death. A typical IRE pulse is presented in Figure 3A, in which the energized electrode would experience an applied voltage 100 µs in duration, repeating once every second.

Unlike thermal ablation techniques, such as radiofrequency ablation and cryoablation, IRE is not thermally driven. As will be discussed later in this chapter, numerical models are used for treatment planning purposes, in which IRE volumes and temperature changes are calculated. A study conducted by Garcia et al. demonstrated numerically that applying ninety 100 µs pulses produces minimal thermal damage. In this study, a statistical model that incorporated dynamic electrical conductivity was used to simulate cell kill due to IRE as well as thermal damage. Results suggested that for tissues with lower electrical conductivities, ranging between 0.067 and 0.241 S/m, necrotic tissue volume produced via Joule heating was only 1.3% of the total ablation volume produced by IRE. Using higher electrical conductivity values, 1.75 times greater, resulted in a percentage of 6.1%, in which the thermally induced necrotic tissue was located at the electrode/tissue interface (19, 20).

In addition to the treatment of brain tumors, IRE has been implemented to treat human patients with prostate (21, 22), pancreatic (23–25), liver (26–28), and kidney (29, 30) tumors. Benefits of IRE therapy include elimination of cytotoxic effects, sharp delineation between treated and spared tissue, a nonthermal mechanism of ablation, treatment planning abilities, sparing of nerves and major blood vessels (31, 32), and, if desired, it can be used as a combinatorial treatment with CT and/or RT. Although effective, RE and IRE are known to cause

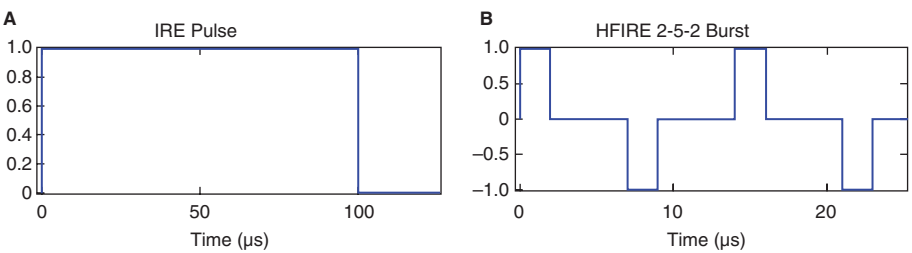

Figure 3 IRE and H-FIRE pulse waveforms. (**A**) IRE and RE treatments typically utilize 100 µs pulses to achieve cell permeabilization while maintaining relatively low thermal damage. (**B**) H-FIRE waveforms are given in positive-rest-negative burst schemes and achieve similar effects to IRE. Comparison between IRE and H-FIRE waveforms is usually done by counting the on-time per pulse period. In this case, the 2-5-2 burst would be repeated until 100 µs of on-time has elapsed.

muscle contractions during treatment, necessitating the use of neuroparalytic agents (33). This poses additional concerns for anesthesiologists, as the dosage of neuroparalytics must be continually monitored to ensure adequate muscle relaxation and proper respiratory function (34). Also, due to changes in electrical conductivity of the tissue during IRE and the heterogeneous nature of tissue on a microscale, treatment planning for IRE can be challenging. Studies have confirmed possible "electric field sink" effects which distort electric field distributions near blood vessels and may lead to undertreatment of tumor tissue (35, 36). Infusing the blood vessels with lower conductivity fluids helps to alleviate the sharp transition from lower conductivity to higher conductivity tissues, but this may be cumbersome and impractical in a clinical setting. To address these challenges associated with RE and IRE, our group developed a novel method of electroporation that utilizes high-frequency bursts to induce electroporation effects.

HIGH-FREQUENCY IRREVERSIBLE ELECTROPORATION

Pulse generators capable of delivering new IRE waveforms have been developed to alleviate the concerns associated with neuroparalytic agents and to simplify treatment planning (37). Namely, these high-frequency IRE (H-FIRE) systems split the ~100 µs unipolar pulse into a series of shorter duration ~1 µs pulses of alternating polarity (Figure 3B). According to classic literature on electrical stimulation, a bipolar pulse has a higher current threshold for action potential excitation as compared to a unipolar pulse of equivalent phase duration (38). This effect is enhanced as pulse duration is reduced. When a microsecond order pulse is applied, there is a latency period between the offset of the pulse and the rising phase of the action potential. A rapid reversal of polarity falling within this latency period can accelerate passive repolarization and inhibit action potential generation (39). An example of this phenomenon is shown in Figure 4, which was derived based on the Hodgkin–Huxley set of partial differential equations for modeling nerve stimulation (40).

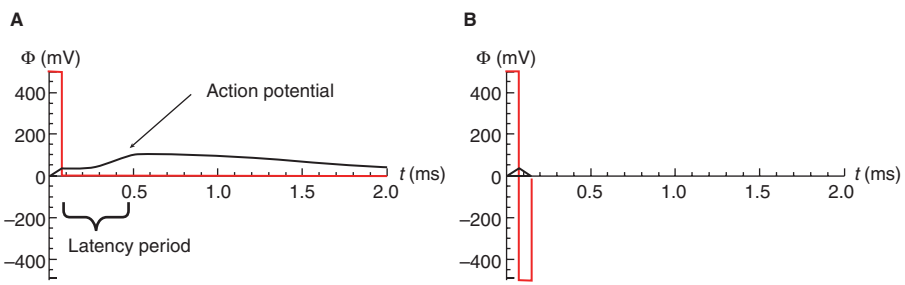

Figure 4 Illustration of action potential inhibition by polarity reversal. (**A**) Unipolar pulse with an amplitude of 500 mV and duration of 75 µs. (**B**) Bipolar pulse with an amplitude of 500 mV and duration of single polarity of 75 µs. This simulation of the Hodgkin–Huxley model was performed in Mathematica 9.0 using parameter values. (Adapted from Bull Math Biol 1952;52(1–2):25–71.)

Following membrane charging, pore formation occurs in the order of ~10 ns (10) and with no latency period. Therefore, it is possible to first induce electroporation and subsequently inhibit muscle contractions by reversing pulse polarity. The first *in vivo* study on H-FIRE was conducted in healthy rat brain (37). Muscle contractions were monitored by placing an accelerometer at the cervicothoracic junction and inserting electrodes into the center of the forelimb area of the sensorimotor cortex. A total of 180 bursts with a total on-time of 200 µs were delivered, and the individual pulse duration comprising each burst varied between 1, 2, and 200 µs for the IRE control. No visual or tactile evidence of muscle contraction was seen during H-FIRE with 1 µs or 2 µs pulses, while the IRE protocol resulted in detectable movement. In addition, H-FIRE produced ablative lesions in brain tissue that were characteristic of IRE treatments, with complete uniformity of tissue death and a sharp transition zone between lesioned and normal brain.

The cell-killing effects of H-FIRE were later explored using 3D *in vitro* tumor constructs and *in vivo* subcutaneous murine tumors over a wide range of pulse durations (250 ns–100 µs) (41). The *in vitro* tumor constructs were assembled by mixing murine pancreatic tumor cells with collagen I hydrogel, injecting into cylindrical molds, and polymerizing at 37°C (42); the *in vivo* subcutaneous tumors were produced by injecting human GBM cells (DBTRG-05MG) into the dorsolateral flank region of athymic nude-Foxn1^{nu} mice. The *in vitro* tests revealed electric field thresholds for cell death of 2022, 1687, 1070, 755, 640, 629, and 531 V/cm for 80 bursts containing 0.25, 0.5, 1, 2, 5, 10, and 50 µs pulses, respectively. *In vivo*, tumor growth was significantly inhibited and all protocols tested (1, 2, and 5 µs pulses) were able to achieve complete regressions. Localized muscle twitching in the treated limb was evident in mice, due to their relatively small size and mass. When similar treatments (5 µs pulses) were applied to spontaneous tumors in equine patients, no movement was observed.

As compared to IRE, H-FIRE waveforms are capable of producing more predictable ablation volumes. The theoretical basis for this argument is twofold. First, the electrical properties of various tissue types converge at high frequencies, and H-FIRE waveforms are comprised of predominately high-frequency components. For example, in a skin-fold geometry, the ratio between the electrical conductivity of fat and skin is 2.25 at 1 MHz (0.027 S/m divided by 0.012 S/m) and 83 at 100 Hz (0.015 S/m divided by 0.00018 S/m) (43). Numerical models have shown that an H-FIRE burst with 500 ns pulses (1 MHz carrier frequency) produces a nearly homogenous electric field distribution across a skin fold (44). This logic can be extended to other heterogeneous tissues, such as the pancreas and brain. Second, electroporation is an active process and the electric conductivity of the tissue increases as pores form and expand. When performing IRE treatments, this step-like change in conductivity must be known *a priori* (45), or measured in real time (46), in order to accurately predict the ablation volume. For H-FIRE waveforms, there is a smaller difference between the pre-treatment and post-treatment conductivities due to capacitive coupling. Bhonsle et al. has shown that the electric field distribution during H-FIRE resembles a theoretical approximation based on the Laplace equation, and the ablation volume can be predicated without additional knowledge of dynamic tissue properties. To demonstrate this phenomenon, IRE and H-FIRE ablations were induced in potato tuber, a proven alternate for studying bioelectric effects of electroporation, and results are shown in Figure 5 (47, 48).

Figure 5 IRE versus H-FIRE ablations in potato tuber. A qualitative comparison between an IRE ablation and an H-FIRE ablation created using a single bipolar probe. (**A**) IRE was induced with 80 pulses energized for 100 µs at 1000 V. (**B**) Laplace solution for the electric field distribution at an arbitrary electric field magnitude, assuming static electrical conductivity. (**C**) H-FIRE was induced with 140 bursts, using a burst scheme of 2-5-2 µs at 1300 V. Typical H-FIRE protocols require higher voltages and more bursts to produce lesion volumes comparable to IRE.

While studying the time course of membrane charging during H-FIRE, Sano et al. recognized that the inter-pulse delay can be tuned to maximize the TMP across the nuclear envelope. Specifically, a delay of 140 ns or less causes the nuclear TMP to double due to compounding effects from pulse falling edges and rising edges (49). In addition, metastatic cells with a larger nucleus-to-cytoplasm ratio can achieve even greater nuclear TMP. In terms of overall cell killing, Pakhomov et al. demonstrated that using bipolar nanosecond electric pulses with sub-microsecond inter-pulse delays induces somewhat of a cancellation effect, resulting in higher lethal thresholds (50). However, a greater inter-pulse delay can lower the threshold for cell death. At 3.7 kV/cm, cell viability was similar when comparing a 300 ns monopulse and a 300–300 ns bipolar pulse with a 10 µs interpulse delay. This illustrates a trade-off between potential selectivity and the overall field threshold required for cell death.

Using the 3D *in vitro* tumor constructs, Ivey and Latouche et al. experimentally validated the selectivity claim (51). In this study, U-87 human GBM cells, DBTRG human GBM cells, C6 rat GBM cells, normal human astrocytes (NHA), normal rat astrocytes D1TNC1, and undifferentiated rat neurons PC12 were cultured in collagen hydrogels and H-FIRE therapy was delivered using a 1-5-1 µs burst scheme. Using numerical models, individual lethal thresholds were determined by overlaying appropriate contours over the lesion. Experimental results showed statistically lower lethal threshold for malignant cells as opposed to healthy cells. Lethal thresholds for U-87, DBTRG, C6, NHA, D1TNC1, and PC 12 were 601, 720, 752, 1006, 1107, and 1076 V/cm, respectively. H-FIRE treatment on hydrogel cocultures of healthy and malignant cells also demonstrated selectivity through partial sparing of healthy tissue. Upon clinical translation, H-FIRE has the potential to kill infiltrative cells beyond the tumor margin while minimizing damage to healthy cells.

BLOOD–BRAIN BARRIER DISRUPTION WITH IRE AND H-FIRE

Difficulties arising from treating MGs with conventional chemotherapy are partly due to protection from the BBB, where the BBB prevents the delivery of these drugs. The BBB is a network of tight junctions that mitigates the transport of large molecules, thereby not only protecting the brain from infections but also hindering the efficacy of chemotherapeutic drugs (52). Garcia et al. demonstrated that

IRE can be applied to the brain not only to ablate tissue but also to cause a transient focal disruption of the BBB, thereby providing a pathway for chemotherapeutics to penetrate (53). For this study, 21 mice received IRE therapy from two monopolar caliper electrodes, measuring 0.45 mm in diameter and 1 mm in exposure with spacing of 4 mm. BBB permeabilization was visualized using Evan's Blue (EB) dye for histological examinations and Gadolinium (Gd) for MR imaging, where EB would represent increased uptake of higher molecular weight compounds, such as proteins, and Gd would represent increased uptake of ions. Results demonstrated that permeability of EB and Gd increased linearly as a function of electric field magnitude, in which 400 V/cm served as a lower threshold, signifying a difference between inducing BBB disruption and IRE ablation. This difference in threshold manifests as having a larger volume of BBB disruption than IRE ablation, as depicted in Figure 2. It was also concluded that BBB disruption is transient due to decreased uptake of both EB and GD if these agents are administered 30 min after IRE treatment, as opposed to administration within 5 min of treatment.

Alternatively, Arena et al. investigated BBB disruption using H-FIRE waveforms (54). The experimental methods, in terms of electrode design and detection of BBB disruption using EB and Gd, were similar to the study mentioned above. High-frequency PEFs were applied to the superficial cerebral cortex of 18 male rats outfitted with a 3-axis accelerometer, as shown in Figure 6. It was discovered that electric field magnitudes of 250 and 2000 V/cm did not induce any muscle

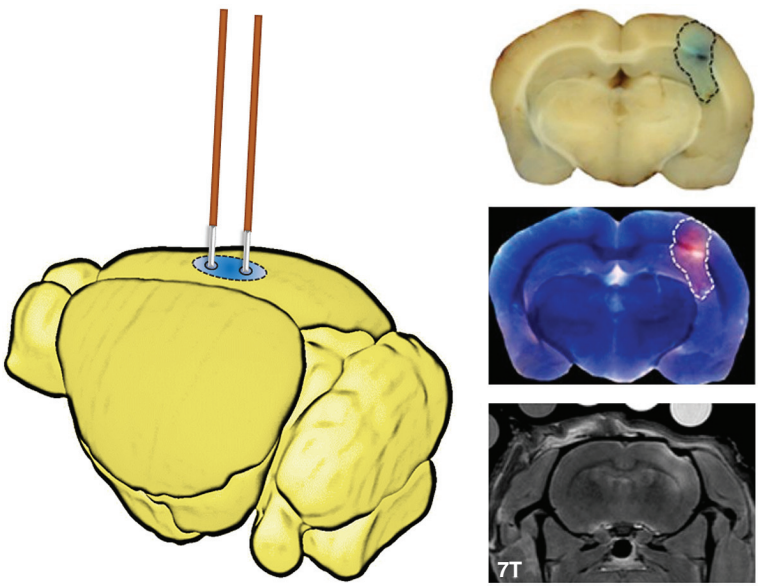

Figure 6 BBB disruption using H-FIRE waveforms. Schematic of BBB disruption using high-frequency PEFs (left), and pathology and MRI evidence of BBB disruption (right). The results are shown for 300 bursts of 0.5 μs bipolar pulses at an applied field of 250 V/cm. The dashed lines depict the limits of BBB disruption. (Adapted from Technology 2014;2(3):206.)

contractions for pulse widths of 0.5 and 2 μs, although visual inspections determined lack of muscle contraction for the 2000 V/cm group because of electrical interference with the accelerometer. Using the lowest energy setting, consisting of 300 bursts and an electric magnitude of 250 V/cm, a BBB disruption zone of 0.51 cm^3 was induced. More importantly, there was no evidence of tissue damage from the high-frequency PEFs, except the physical damage due to electrode insertion. However, if the number of bursts is increased to 600, there is significant cell death with no increase in BBB disruption zone, indicating a maximum energy threshold to disrupting BBB while not sustaining damage by high-frequency PEFs. The total charge delivered with IRE pulses and H-FIRE bursts is typically compared to the charge delivered during electroconvulsive therapy (33) due to the ultrashort duration of these pulses/bursts.

The data presented indicate that both IRE and H-FIRE can be optimized to promote cell death via ablation mechanism and simultaneously disrupt the BBB, allowing adjuvant therapies to reach the infiltrative cell region in GBM. Most notably, H-FIRE has been shown to extend BBB disruption without causing cell death. Additional benefits of H-FIRE include no induced muscle contractions, targeted malignant cellular ablation, and more predictable ablation geometries. Although not discussed, investigations for permeabilization of the BBB have also been performed *in vitro* (55).

IRE AND H-FIRE TREATMENT PLANNING

Treatment planning for IRE and H-FIRE can be accomplished using a finite element package, for example, COMSOL Multiphysics 5.2a (Stockholm, Sweden). The degree of electroporation is dependent on the electrical impedance distribution, electric field distribution, electrode and tissue geometries, and pulsing parameters such as pulse width, number of pulses, and inter-pulse delay. Maxwell's equations are a set of partial differential equations that form the foundation of electromagnetism. The fundamental equations for solving the electric field distribution of IRE and H-FIRE include Faraday's Law and Ampere's Law:

$$\nabla \times \vec{E} = -\frac{\partial \vec{B}}{\partial t} \quad [1]$$

$$\nabla \times \vec{H} = \vec{J} + \frac{\partial \vec{D}}{\partial t} \quad [2]$$

where $\vec{E}$ is the electric field, $\vec{B}$ is the magnetic field, $\vec{H}$ is the auxiliary magnetic field, $\vec{J}$ is the total current density, and $\vec{D}$ is the displacement current density. By taking the divergence of Ampere's Law, equation 2, and substituting constitutive equations, we obtain the following:

$$\nabla \cdot \left(\sigma \vec{E}\right) + \frac{\partial}{\partial t}\left(\nabla \cdot \left(\varepsilon \vec{E}\right)\right) = 0 \quad [3]$$

where σ is the electrical conductivity and ε is the dielectric permittivity. Using the electroquasistatic approximation for Faraday's Law, equation 1, in which the magnetic field can be considered negligible in contributing to the displacement of electrical charge, we can describe the electric field in terms of an electric potential, φ:

$$\nabla \times \vec{E} = 0 \quad [4]$$

$$\vec{E} = -\nabla\varphi \quad [5]$$

Thus, by combining equations 3 and 4 and assuming steady state, we can rewrite this equation as:

$$-\nabla \cdot (\sigma \cdot \nabla\varphi) = 0 \quad [6]$$

$$\sigma = f\left(\vec{E}\right) \quad [7]$$

For IRE, boundary conditions are applied to the electrode/tissue interface in which one electrode is energized at a voltage V_0 and the other is grounded, while in the case of H-FIRE, the boundary conditions would need to be alternated between each electrode due to the rapid reversal of polarity. The remaining boundaries are treated as electrically insulating. For the thermal boundary and initial conditions, we assume an adiabatic boundary to calculate the maximum possible temperature increase and an initial temperature of T_0.

Using these equations, it is possible to map the electric field distribution and predict volumes of electroporated heterogeneous dynamic tissue for use in clinical application. It has been largely accepted that changes in electrical conductivity due to electroporation is a dynamic phenomenon (18–20, 25, 56). Accounting for dynamic conductivity allows for more accurate representation of lesions created by IRE (57), and potentially H-FIRE. Incorporating changes in tissue conductivity can be achieved using a fitted Gompertz function (58). Alternatively, a sigmoid function can mimic changes in electrical conductivity due to electric field magnitude as well as temperature. Garcia et al. incorporated the following equation for analysis of IRE ablations in intracranial tissue (20):

$$\sigma\left(E,T(t)\right) = \sigma_0 \cdot \left[1 + 2 \cdot flc2hs\left(E_{norm} - E_{Delta}, E_{range}\right) + \alpha \cdot \left(T(t) - T_0\right)\right] \quad [8]$$

where σ_0 represents the initial electrical conductivity, *flc2hs* is a Heaviside function, α is the temperature coefficient, E_{norm} represents the norm of the electric field, and E_{delta} and E_{range} are coefficients pertaining to the electric field thresholds required for conductivity changes.

Temperature changes due to resistive heating from pulsing, Joule heating, can also be incorporated into numerical models. Joule heating and blood perfusion are modeled through a modified Pennes' Bioheat equation:

$$\nabla \cdot \left(k\nabla T\right) - \omega_b C_b \rho_b \left(T - T_a\right) + q''' + \sigma\left|\nabla\varphi\right|^2 = \rho C_p \frac{\partial T}{\partial t} \quad [9]$$

where $\sigma|\nabla\varphi|^2$ is the Joule heating term, k is the thermal conductivity, ω_b is the blood perfusion rate, C_b is the blood-specific heat capacity, ρ_b is the density of blood, T_α is the arterial blood temperature, q''' is the metabolic heat generation, ρ is the density of the tissue, and C_p is the specific heat capacity of the tissue. Rather than simulating hundreds of IRE or H-FIRE pulses, a modified duty cycle approach is applied to ease the computational burden (20). We can rewrite this modified Bioheat equation as:

$$\nabla\cdot\left(k\nabla T\right)-\omega_b C_b\rho_b\left(T-T_a\right)+q'''+\frac{\tau\left(\sigma\left|\vec{E}\right|^2\right)}{P}=\rho C_p\frac{\partial T}{\partial t} \qquad [10]$$

where τ represents the on-time per pulse and P is the period per pulse. For example, if a 50 µs pulse was repeated every 0.5 s, the ratio would equal to 100 µs. This simplification has proven effective in representing the energy associated with intra-pulse heating, as a constant heat source acting over the period of one pulse.

In addition, thermal damage analysis can be incorporated by adding a thermal damage equation:

$$(t)=\int_0^\tau \zeta e^{-\frac{E_a}{R*T(t)}}dt \qquad [11]$$

where ζ represents the frequency factor, E_a the activation energy, R the universal gas constant, and τ the total time of heating (59). For the values in Table 1, an Ω value of 1 correlates to tissue coagulation.

As an example, the results of Garcia et al. were replicated using monopolar electrodes inserted into a homogeneous medium. A human brain and tumor were segmented using 3D Slicer 4.6 (Boston, United States) (60–64), and imported into COMSOL. The dynamic conductivity function was applied in COMSOL with σ_0 = 0.256 S/m, σ_{max} = 0.768 S/m, E_{delta} = 580 V/cm, and E_{range} = ± 120 V/cm. However, in the thermal damage calculations, a zeta of 7.39×10^{39} was used for protein coagulation. The value of α was set to zero because of the relatively low increase in temperature. The spacing and electrode exposure were set to 2.5 cm and a voltage of 2500 V was applied to maintain a 1000 V/cm electric field magnitude. It is important to note that more accurate models will incorporate the separation of white and gray matter, as well as account for the anisotropy in white matter. Nonetheless, even simple numerical models such as this one can provide clinicians with valuable information regarding heat generation during pulsing as well as estimates for ablation volumes before performing the procedure *in vivo*. The results show the tumor mostly engulfed within lethal IRE thresholds, while causing minimum temperature changes at the midpoint between the electrodes (Table 2). Due to the abnormally large tumor size, 18.81 cm^3, two sets of pulses were simulated in which the electrode depth was moved vertically 2 cm to allow sufficient treatment. Although the entire tumor is not within the ablation zone, adjuvant chemotherapy can be utilized in the BBB disruption zone as discussed previously. For large, irregular tumors, it is not unusual to use more than two electrode pairs, while for smaller tumors, the bipolar probe, as shown in Figure 2B,

TABLE 1 Material Properties and Parameters

Material	Property	Symbol	Value	Units	Reference
Brain	Thermal conductivity	k	0.565	$W \cdot m^{-1} \cdot K^{-1}$	(70)
	Heat capacity	C_p	3680	$J \cdot kg^{-1} \cdot K^{-1}$	(70)
	Density	ρ	1039	$kg \cdot m^{-3}$	(70)
	Temperature coefficient	α	0.032	$^{o}C^{-1}$	(70)
	Metabolic heat generation	q'''	10,437	$W \cdot m^{-3}$	(20)
Blood	Heat capacity	C_b	3840	$J \cdot kg^{-1} \cdot K^{-1}$	(20)
	Density	ρ	1060	$kg \cdot m^{-3}$	(20)
	Blood perfusion rate	ω_b	7.15×10^{-3}	S^{-1}	(20)
Insulation	Electrical conductivity	σ	1.0×10^{-5}	$S \cdot m^{-1}$	(71)
	Thermal conductivity	k	0.01	$W \cdot m^{-1} \cdot K^{-1}$	(71)
	Heat capacity	C_p	3400	$J \cdot kg^{-1} \cdot K^{-1}$	(71)
	Density	ρ	800	$kg \cdot m^{-3}$	(71)
Stainless steel	Electrical conductivity	σ	2.22×10^{6}	$S \cdot m^{-1}$	(20)
	Thermal conductivity	k	15	$W \cdot m^{-1} \cdot K^{-1}$	(71)
	Heat capacity	C_p	500	$J \cdot kg^{-1} \cdot K^{-1}$	(71)
	Density	ρ	7900	$kg \cdot m^{-3}$	(71)

TABLE 2 Temperature Profile at Various Time Points

Time [s]	T_{mid} [K]	$T_{electrode}$ [K]
0	310.15	310.15
10	310.53	315.23
20	310.87	317.51
30	311.18	319.08
40	311.47	320.15
50	311.73	320.99
60	311.97	321.66
70	312.19	322.18
80	312.40	322.60
90	312.59	322.95
100	312.42	318.31
130	312.01	314.15
160	311.70	312.58

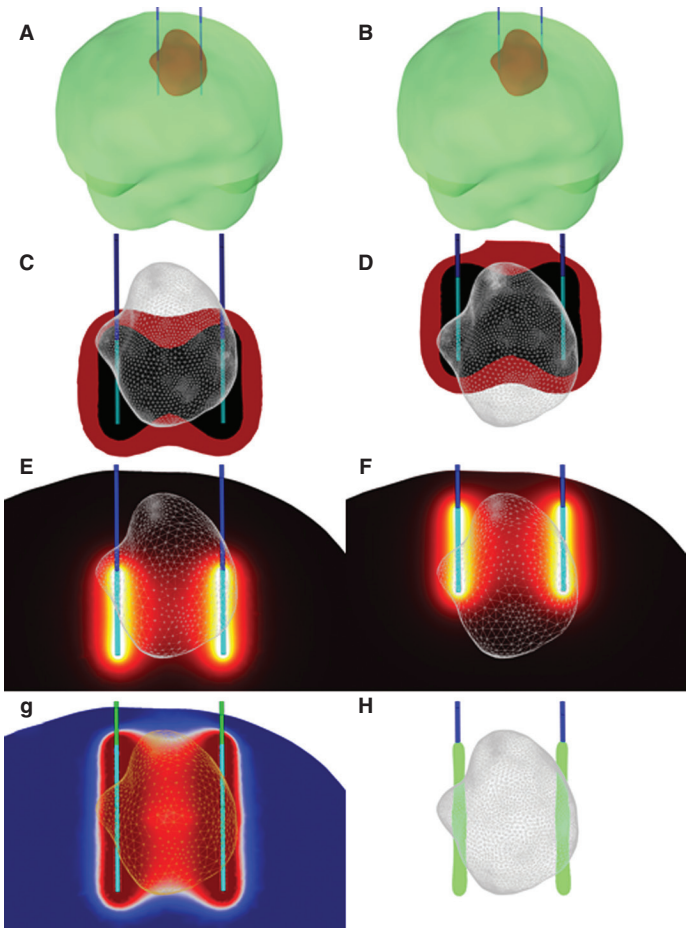

Figure 7 Results of IRE therapy in 3D reconstruction of a human brain. Results from IRE therapy with monopolar electrodes (1 mm diameter, 2.5 cm exposure, 2.5 cm spacing) in a segmented brain and tumor (**A**, **B**) showing the electric field (**C**, **D**), temperature (**E**, **F**), and the effective electrical conductivity distribution (**G**), as well as the thermal damage (**H**). Ninety 50 µs pulses were delivered at voltage-to-distance ratio of 1000 V/cm (applied voltage of 2500 V). A damage integral of Ω (t)= 1 corresponds to a 63% probability of cell death. The simulation parameters were identical to those used by Garcia et al. (20), except that the frequency factor of $7.39 \times 1039\ S^{-1}$ was used for thermal damage associated with protein coagulation. Maximum temperature during treatment was 322.95 K.

has proven to be effective (24). The results of this simulation, Figure 7, demonstrate a maximum temperature change of about 12°C at the electrode surface, and 2°C in between the electrodes.

Treatment planning for both IRE and H-FIRE can be accomplished using the method described previously. Adapting to either IRE or H-FIRE would mean that the conductivity values would change depending on which method is being employed. As mentioned earlier, the ratio of conductivities between different

tissues converges when using higher frequency waveforms; thus, H-FIRE will produce lesions that are more closely approximated by electric fields in static conductivity mediums.

IRE/H-FIRE PRECLINICAL ANIMAL TRIALS

When applying IRE to the liver, kidney, prostate, and pancreas, it is important to maintain a high IRE to thermal ablation ratio. For example, a temperature increase between 10°C and 15°C at the electrode/tissue interface is considered not to cause significant thermal damage to the surrounding tissue. As calculated previously, a 12°C increase at the electrode/tissue interface correlated to a 2°C increase at the midpoint of the electrodes, indicating the tissue exposed to higher temperatures is localized at this interface. Like other organs, the brain is also susceptible to fluctuations in temperature, thus preliminary studies aimed to numerically validate the use of nonthermal IRE (N-TIRE), where pulse parameters are tuned to eliminate most thermal effects.

Studies were conducted to elucidate the lethal threshold for dog GBM cell line J3T (65). As opposed to using 100 µs pulses, Neal et al. utilized 50 µs pulses to minimize the energy delivered while still maintaining electroporation effects. 96-well electroporation plates seeded with J3T cells were electroporated using combinations of 1000 and 1500 V/cm electric fields and 10, 30, 50, and 70 pulses. A WST-1 reagent was used to quantify cell viability, where an absorbance of 0.2 would indicate 100% cell death. It was concluded that IRE can be achieved by applying 50 pulses at 1000 V/cm, absorbance of 0.229, without incurring significant thermal damage.

Rossmeisl and Garcia et al. aimed to verify *in vitro* studies by performing IRE therapy in seven canines with spontaneous brain tumors (66). Canines are preferred translational models because they develop brain cancers three times more often than their human counterparts. Canine gliomas also show similar biologic, pathologic, and molecular properties as human gliomas do, thus making them an acceptable translational model (see Part V, page xxx) (67). Prior to the application of IRE, pre-treatment planning models were developed and used to determine pulse parameters and electrode configurations. From these models, total ablation protocols were created for tumors smaller than 2.5 cm^3 and volume reduction protocols were created for those larger than 2.5 cm^3. A craniectomy defect is introduced to allow placement of blunt tip electrodes into the gray matter. Prior to procedure, atracurium, a neuromuscular blockade, is administered to suppress muscle contraction during the onset of pulses. A range of pulses between 90 and 270 were delivered at electric field magnitudes ranging between 1000 and 2000 V/cm in sets consisting of 10 and 20 pulses. After each set of pulses, the polarity was reversed to minimize charge build up, which has become customary when doing these procedures. Brain edema was noticed in one dog during IRE treatment but was resolved by administering corticosteroids and diuretics. MRI confirmed a sharp delineation between treated and healthy tissue, as well as signs of BBB disruption. Common adverse events occurring after IRE treatment included seizure, vomiting, and diarrhea, although one dog developed fatal aspiration pneumonia. In the six canines that survived, the median Karnofsky Performance Scale score increased from 70 to 80, 14 days post-IRE treatment.

Ellis et al. performed IRE in four canines, of which one dog served to find an upper safety limit when applying higher voltages (68). Nine sets of ten 50 µs pulses were delivered at a rate of 4 Hz. Like before, polarities were alternated after the completion of each set which were delivered at electric field magnitudes of 1000 and 2000 V/cm. Similar results were achieved as in the previous study, except in the case of the canine undergoing higher voltage treatment. Higher voltage pulses resulted in coagulative necrosis of tissue located within the treatment zone, which led to arterial thrombosis and lacunar infarction. Canines that received treatment at 1600 V produced lesion volumes of ~1.655 cm^3 while maintaining a thermal isoeffective dose of 5.6 min. The canine that received higher voltage treatment experienced an isothermal dose over 60 min, where doses over 60 min correlate to neuronal damage. Based on *in vivo* data from this study, Garcia et al. backed out lethal thresholds using numerical models which incorporated dynamic electrical conductivity dependent on electroporation and temperature effects (33). It was concluded that lethal thresholds for healthy canine brain tissue are 495 and 510 V/cm for applied voltages of 500 and 1000 V, respectively.

Studies have also confirmed nonthermal ablation in deep-seated tumors (33). This ablation was performed primarily in white matter, which, using *in vivo* measurements, was calculated to have higher conductivity, σ = 0.35 S/m, than what has been determined for gray matter. Numerical simulations which incorporated dynamic conductivity predicted lethal thresholds for white matter to be 630–875 V/cm. In the clinic, this translates to having to apply slightly higher voltages to treat deep-seated tumors.

Combinatorial IRE treatments have also been studied. Garcia et al. applied IRE therapy and adjuvant RT to a 12-year-old mixed breed dog with an 8-week history of partial seizures and behavioral changes (69). Numerical treatment planning for IRE incorporated dynamic conductivity changes, and from these simulations, it was determined that two groups of pulses would be delivered. The first group consisted of four sets of twenty 50 µs pulses and the second group of two sets of twenty 50 µs pulses, with an applied voltage of 650 and 500 V, respectively. No adverse clinical effects were observed, and 48 h after treatment, the size of the neoplasm was reduced 75% in size. It was concluded that the lethal threshold for malignant tissue is much lower than that of healthy tissue, implying some sort of selectivity in the brain. Five days after N-TIRE treatment, the patient's neurologic status improved and the previously noted aggression improved. Sixteen days postoperation, the canine received 50 Gy of fractionated RT delivered in 20 treatment sessions, each consisting of 2.5 Gy. Upon completion of radiotherapy, the patient showed evidence of cognitive dysfunction, disturbed sleep–wake cycle, and lack of awareness of familiar people. At 4.5 months post-IRE, the patient showed acute deterioration in mentation and circling to the left. Clinical and MRI results suggested early delayed radiation encephalopathy. At the owner's request, the patient was euthanized. The patient had an overall survival of 149 days after N-TIRE therapy. Postmortem exam showed no evidence of recurrent MG. H-FIRE was also shown to be safe when applied without the use of neuroparalytics and was capable of destroying brain tumors, although these exploratory treat and resect studies are currently ongoing.

Conclusion

The use of IRE and H-FIRE in treating unresectable tumors has been supported by *in vivo*, *ex vivo*, and *in vitro* studies. These therapies have demonstrated their effectiveness in eradicating tumors of the kidney, prostate, pancreas, liver, and, most importantly, the brain in animal models. Benefits of utilizing H-FIRE for treating GBM include sparing of major blood vessels and nerves, focal BBB disruption, selectivity toward malignant cells, more predictable ablation geometries due to mitigation of impedance changes, lack of muscle contractions, and nonthermal ablation.

Acknowledgment: The authors would like to thank Temple Douglas, Maltish Lorenzo, Natalie White, Philip Graybill, Suyashree Bhonsle, Dan Sweeney and Elisa Wasson for their help in editing and providing feedback for writing this chapter. The authors also thank the NIH (R01CA213423 High-Frequency IRE for combinatorial GBM treatment) for funding and general support of this research.

Conflict of Interest: Dr. Davalos and Dr. Arena have patents in the fields of irreversible electroporation and high-frequency irreversible electroporation.

References

1. Zhang X, Zhang W, Cao W-D, Cheng G, Zhang Y-Q. Glioblastoma multiforme: Molecular characterization and current treatment strategy (Review). Exp Ther Med. 2012;3(1):9–14.
2. Henriksson R, Asklund T, Poulsen HS. Impact of therapy on quality of life, neurocognitive function and their correlates in glioblastoma multiforme: A review. J Neurooncol. 2011;104(3):639–46. http://dx.doi.org/10.1007/s11060-011-0565-x
3. Glas M, Happold C, Rieger J, Wiewrodt D, Bixhr O, Steinbach JP, et al. Long-term survival of patients with glioblastoma treated with radiotherapy and lomustine plus temozolomide. J Clin Oncol. 2009;27(8):1257–61. http://dx.doi.org/10.1200/JCO.2008.19.2195
4. Mitragotri S. Healing sound: The use of ultrasound in drug delivery and other therapeutic applications. Nat Rev Drug Discov. 2005 4(3):255–60. http://dx.doi.org/10.1038/nrd1662
5. Mehier-Humbert S, Bettinger T, Yan F, Guy RH. Plasma membrane poration induced by ultrasound exposure: Implication for drug delivery. J Control Release. 2005;104(1):213–22. http://dx.doi.org/10.1016/j.jconrel.2005.01.007
6. Liu J, Lewis TN, Prausnitz MR. Non invasive assessment and control of ultrasound-mediated membrane permeabilization. Pharmaceut Res. 1998;15:918–24. http://dx.doi.org/10.1023/A:1011984817567
7. Neu W, Neu J. Theory of electroporation. In: Efimov IR, Kroll MW, Tchou PJ, editors. Cardiac bioelectric therapy mechanisms. NY: Springer; 2015. p. 133–61.
8. Weaver JC. Electroporation: A general phenomenon for manipulating cells and tissues. J Cell Biochem. 1993;51(4):426–35. http://dx.doi.org/10.1002/jcb.2400510407

9. Sweeney DC, Reberšek M, Dermol J, Rems L, Miklavčič D, Davalos RV. Quantification of cell membrane permeability induced by monopolar and high-frequency bipolar bursts of electrical pulses. Biochim Biophys Acta Biomembr. 2016;1858(11):2689–98.
10. Böckmann RA, de Groot BL, Kakorin S, Neumann E, Grubmüller H. Kinetics, statistics, and energetics of lipid membrane electroporation studied by molecular dynamics simulations. Biophys J. 2008;95(4):1837–50. http://dx.doi.org/10.1529/biophysj.108.129437
11. Miklavčič D, Mali B, Kos B, Heller R, Serša G. Electrochemotherapy: From the drawing board into medical practice. Biomed Eng Online. 2014;13(1):29. http://dx.doi.org/10.1186/1475-925X-13-29
12. André F, Mir LM. DNA electrotransfer: Its principles and an updated review of its therapeutic applications. Gene Ther. 2004;11(Suppl 1):S33–42. http://dx.doi.org/10.1038/sj.gt.3302367
13. Agerholm-Larsen B, Iversen HK, Ibsen P, Moller JM, Mahmood F, Jensen KS, et al. Preclinical validation of electrochemotherapy as an effective treatment for brain tumors. Cancer Res. 2011;71(11): 3753–62. http://dx.doi.org/10.1158/0008-5472.CAN-11-0451
14. Gothelf A, Mir LM, Gehl J. Electrochemotherapy: Results of cancer treatment using enhanced delivery of bleomycin by electroporation. Cancer Treat Rev. 2003;29(5):371–87. http://dx.doi.org/10.1016/S0305-7372(03)00073-2
15. Frandsen SK, Gissel H, Hojman P, Eriksen J, Gehl J. Calcium electroporation in three cell lines: A comparison of bleomycin and calcium, calcium compounds, and pulsing conditions. Biochim Biophys Acta Gen Subj. 2014;1840(3):1204–8. http://dx.doi.org/10.1016/j.bbagen.2013.12.003
16. Frandsen SK, Gissel H, Hojman P, Tramm T, Eriksen J, Gehl J. Direct therapeutic applications of calcium electroporation to effectively induce tumor necrosis. Cancer Res. 2012;72(6):1336–41. http://dx.doi.org/10.1158/0008-5472.CAN-11-3782
17. Davalos RV, Mir LM, Rubinsky B. Tissue ablation with irreversible electroporation. Ann Biomed Eng. 2005;33(2):223–31. http://dx.doi.org/10.1007/s10439-005-8981-8
18. Edd JF, Davalos R V. Mathematical modeling of irreversible electroporation for treatment planning. Technol Cancer Res Treat. 2007;6(4):275–86. http://dx.doi.org/10.1177/153303460700600403
19. Garcia PA, Davalos RV., Miklavcic D. A numerical investigation of the electric and thermal cell kill distributions in electroporation-based therapies in tissue. PLoS One. 2014;9(8):e103083. http://dx.doi.org/10.1371/journal.pone.0103083
20. Garcia PA, Rossmeisl JH, Neal RE, Ellis TL, Davalos RV., Rossmeisl JH, Jr., et al. A parametric study delineating irreversible electroporation from thermal damage based on a minimally invasive intracranial procedure. Biomed Eng Online. 2011;10(1):34. http://dx.doi.org/10.1186/1475-925X-10-34
21. Valerio M, Dickinson L, Ali A, Ramachandran N, Donaldson I, Freeman A, et al. A prospective development study investigating focal irreversible electroporation in men with localised prostate cancer: Nanoknife electroporation ablation trial (NEAT). Contemp Clin Trials. 2014;39(1):57–65. http://dx.doi.org/10.1016/j.cct.2014.07.006
22. Neal RE, Millar JL, Kavnoudias H, Royce P, Rosenfeldt F, Pham A, et al. In vivo characterization and numerical simulation of prostate properties for non-thermal irreversible electroporation ablation. Prostate. 2014;74(5):458–68. http://dx.doi.org/10.1002/pros.22760
23. Martin RCG, McFarland K, Ellis S, Velanovich V. Irreversible electroporation in locally advanced pancreatic cancer: Potential improved overall survival. Ann Surg Oncol. 2013 Nov;20(Suppl 3):443–9.
24. Martin RCG, McFarland K, Ellis S, Velanovich V. Irreversible electroporation therapy in the management of locally advanced pancreatic adenocarcinoma. J Am Coll Surg. 2012;215(3):361–9. http://dx.doi.org/10.1016/j.jamcollsurg.2012.05.021
25. Latouche EL, Sano MB, Lorenzo MF, Davalos RV, Martin RCG. Irreversible electroporation for the ablation of pancreatic malignancies: A patient-specific methodology. J Surg Oncol. 2017 Jan:1–7. http://dx.doi.org/10.1002/jso.24566
26. Cannon R, Ellis S, Hayes D, Narayanan G, Martin RCG. Safety and early efficacy of irreversible electroporation for hepatic tumors in proximity to vital structures. J Surg Oncol. 2013;107(5):544–9. http://dx.doi.org/10.1002/jso.23280
27. Kingham TP, Karkar AM, D'Angelica MI, Allen PJ, Dematteo RP, Getrajdman GI, et al. Ablation of perivascular hepatic malignant tumors with irreversible electroporation. J Am Coll Surg. 2012;215(3): 379–87. http://dx.doi.org/10.1016/j.jamcollsurg.2012.04.029

28. Scheffer HJ, Nielsen K, De Jong MC, Van Tilborg AAJM, Vieveen JM, Bouwman A, et al. Irreversible electroporation for nonthermal tumor ablation in the clinical setting: A systematic review of safety and efficacy. J Vasc Interv Radiol. 2014;25(7):997–1011. http://dx.doi.org/10.1016/j.jvir.2014.01.028
29. Pech M, Janitzky A, Wendler JJ, Strang C, Blaschke S, Dudeck O, et al. Irreversible electroporation of renal cell carcinoma: A first-in-man phase i clinical study. Cardiovasc Intervent Radiol. 2011;34(1):132–8. http://dx.doi.org/10.1007/s00270-010-9964-1
30. Thomson KR, Cheung W, Ellis SJ, Federman D, Kavnoudias H, Loader-Oliver D, et al. Investigation of the safety of irreversible electroporation in humans. J Vasc Interv Radiol. 2011 22(5):611–21. http://dx.doi.org/10.1016/j.jvir.2010.12.014
31. Li W, Fan Q, Ji Z, Qiu X, Li Z. The effects of irreversible electroporation (IRE) on nerves. PLoS One. 2011;6(4):e18831. http://dx.doi.org/10.1371/journal.pone.0018831
32. Maor E, Ivorra A, Leor J, Rubinsky B. The effect of irreversible electroporation on blood vessels. Technol Cancer Res Treat. 2007;6(4):307–12. http://dx.doi.org/10.1177/153303460700600407
33. Garcia PA, Rossmeisl JH, Neal RE, Ellis TL, Olson JD, Henao-Guerrero N, et al. Intracranial nonthermal irreversible electroporation: In vivo analysis. J Membr Biol. 2010;236(1):127–36. http://dx.doi.org/10.1007/s00232-010-9284-z
34. Eikermann M, Groeben H, Hüsing J, Peters J. Accelerometry of adductor pollicis muscle predicts recovery of respiratory function from neuromuscular blockade. Anesthesiology. 2003;98(6):1333–7. http://dx.doi.org/10.1097/00000542-200306000-00006
35. Golberg A, Bruinsma BG, Uygun BE, Yarmush ML. Tissue heterogeneity in structure and conductivity contribute to cell survival during irreversible electroporation ablation by "electric field sinks." Sci Rep. 2015;5:8485. http://dx.doi.org/10.1038/srep08485
36. Qasrawi R, Silve L, Burdío F, Abdeen Z, Ivorra A. Anatomically realistic simulations of liver ablation by irreversible electroporation. Technol Cancer Res Treat. 2017:153303461668747. http://dx.doi.org/10.1177/1533034616687477
37. Arena CB, Sano MB, Rossmeisl JH, Caldwell JL, Garcia PA, Rylander MN, et al. High-frequency irreversible electroporation (H-FIRE) for non-thermal ablation without muscle contraction. Biomed Eng Online. 2011;10(1):102. http://dx.doi.org/10.1186/1475-925X-10-102
38. Patrick Reilly J, Freeman VT, Larkin WD. Sensory effects of transient electrical stimulation—Evaluation with a neuroelectric model. IEEE Trans Biomed Eng. 1985;BME-32(12):1001–11. http://dx.doi.org/10.1109/TBME.1985.325509
39. van den Honert C, Mortimer JT. The response of the myelinated nerve fiber to short duration. Ann Biomed Eng. 1979;7:117–25. http://dx.doi.org/10.1007/BF02363130
40. Hodgkin AL, Huxley AF. A quantitative description of membrane current and its application to conduction and excitation in nerve. Bull Math Biol. 1952;52(1–2):25–71. http://dx.doi.org/10.1113/jphysiol.1952.sp004764
41. Sano MB, Arena CB, Bittleman KR, DeWitt MR, Cho HJ, Szot CS, et al. Bursts of bipolar microsecond pulses inhibit tumor growth. Sci Rep. 2015;5:14999. http://dx.doi.org/10.1038/srep14999
42. Arena CB, Szot CS, Garcia PA, Rylander MN, Davalos RV. A three-dimensional in vitro tumor platform for modeling therapeutic irreversible electroporation. Biophys J. 2012;103(9):2033–42. http://dx.doi.org/10.1016/j.bpj.2012.09.017
43. Andreuccetti D, Fossi R, Petrucci C. An Internet resource for the calculation of the dielectric properties of body tissues in the frequency range 10Hz-100GHz. Institute for Applied Physics, Italian National Research Council. Available from: http://niremf.ifac.cnr.it/tissprop/ (Accessed February 8, 2017).
44. Arena CB, Sano MB, Rylander MN, Davalos RV. Theoretical considerations of tissue electroporation with high-frequency bipolar pulses. IEEE Trans Biomed Eng. 2011;58(5):1474–82. http://dx.doi.org/10.1109/TBME.2010.2102021
45. Davalos RV, Otten DM, Mir LM, Rubinsky B. Electrical impedance tomography for imaging tissue electroporation. IEEE Trans Biomed Eng. 2004;51(5):761–7.
46. Bonakdar M, Latouche EL, Mahajan RL, Davalos RV. The feasibility of a smart surgical probe for verification of IRE treatments using electrical impedance spectroscopy. IEEE Trans Biomed Eng. 2015;62(11):2674–84.

47. Bhonsle SP, Arena CB, Sweeney DC, Davalos RV. Mitigation of impedance changes due to electroporation therapy using bursts of high-frequency bipolar pulses. Biomed Eng Online. 2015;14(Suppl 3):S3.
48. Ivorra A, Mir LM, Rubinsky B. Electric field redistribution due to conductivity changes during tissue electroporation: Experiments with a simple vegetal model. In: Dössel O, Schlegel WC, editors. World Congress on Medical Physics and Biomedical Engineering, September 7–12, 2009, Munich, Germany. IFMBE Proceedings, vol. 25/13. Berlin: Springer.
49. Sano MB, Arena CB, DeWitt MR, Saur D, Davalos RV. In-vitro bipolar nano- and microsecond electropulse bursts for irreversible electroporation therapies. Bioelectrochemistry. 2014;100:69–79. http://dx.doi.org/10.1016/j.bioelechem.2014.07.010
50. Pakhomov AG, Semenov I, Xiao S, Pakhomova ON, Gregory B, Schoenbach KH, et al. Cancellation of cellular responses to nanoelectroporation by reversing the stimulus polarity. Cell Mol Life Sci. 2014;71(22):4431–41. http://dx.doi.org/10.1007/s00018-014-1626-z
51. Ivey JW, Latouche EL, Sano MB, Rossmeisl JH, Davalos RV, Verbridge SS. Targeted cellular ablation based on the morphology of malignant cells. Sci Rep. 2015;5:17157. http://dx.doi.org/10.1038/srep17157
52. Janzer RC, Raff MC. Astrocytes induce blood-brain barrier properties in endothelial cells. Nature. 1987;325:253–7. http://dx.doi.org/10.1038/325253a0
53. Garcia PA, Rossmeisl JH, Robertson JL, Olson JD, Johnson AJ, Ellis TL, et al. 7.0-T Magnetic resonance imaging characterization of acute blood-brain-barrier disruption achieved with intracranial irreversible electroporation. PLoS One. 2012;7(11):1–8. http://dx.doi.org/10.1371/journal.pone.0050482
54. Arena CB, Garcia PA., Sano MB, Olson JD, Rogers-Cotrone T, Rossmeisl JH, et al. Focal blood-brain-barrier disruption with high-frequency pulsed electric fields. Technology. 2014;2(3):1–8. http://dx.doi.org/10.1142/S2339547814500186
55. Bonakdar M, Wasson EM, Lee YW, Davalos RV. Electroporation of brain endothelial cells on chip toward permeabilizing the blood-brain barrier. Biophys J. 2016;110(2):503–13. http://dx.doi.org/10.1016/j.bpj.2015.11.3517
56. Langus J, Kranjc M, Kos B, Šuštar T, Miklavčič D. Dynamic finite-element model for efficient modelling of electric currents in electroporated tissue. Sci Rep. 2016 May;6:26409. http://dx.doi.org/10.1038/srep26409
57. Corovic S, Lackovic I, Sustaric P, Sustar T, Rodic T, Miklavcic D. Modeling of electric field distribution in tissues during electroporation. Biomed Eng Online. 2013;12(1):16. http://dx.doi.org/10.1186/1475-925X-12-16
58. Neal RE, Garcia PA, Robertson JL, Davalos RV. Experimental characterization and numerical modeling of tissue electrical conductivity during pulsed electric fields for irreversible electroporation treatment planning. IEEE Trans Biomed Eng. 201259(4):1076–85. http://dx.doi.org/10.1109/TBME.2012.2182994
59. Tropea BI, Lee RC. Thermal injury kinetics in electrical trauma. J Biomech Eng. 1992;114(2):241–50. http://dx.doi.org/10.1115/1.2891378
60. Brigham and Women's Hospital, 3D Slicer Contributors. 3D Slicer. 2015:1–4. Available from: http://www.slicer.org (Accessed January 16, 2017).
61. Fedorov A, Beichel R, Kalpathy-Cramer J, Finet J, Fillion-Robin JC, Pujol S, et al. 3D Slicer as an image computing platform for the Quantitative Imaging Network. Magn Reson Imaging. 2012;30(9):1323–41. http://dx.doi.org/10.1016/j.mri.2012.05.001
62. Gering DT, Nabavi A, Kikinis R, Hata N, O'Donnell LJ, Grimson WE, et al. An integrated visualization system for surgical planning and guidance using image fusion and an open MR. J Magn Reson Imaging. 2001;13(6):967–75. http://dx.doi.org/10.1002/jmri.1139
63. Gering DT, Nabavi A, Kikinis R, Grimson WEL, Hata N, Everett P, et al. An integrated visualization system for surgical planning and guidance using image fusion and interventional imaging. In: International Conference on Medical Image Computing and Computer-Assisted Intervention, September 1999. Med Image Comput Comput Assist Interv. MICCAI. 1999. p. 809–19.
64. Pieper S, Lorensen B, Schroeder W, Kikinis R. The NA-MIC Kit: ITK, VTK, pipelines, grids and 3D Slicer as an open platform for the medical image computing community. In: IEEE 3rd International Symposium on Biomedical Imaging: Macro to Nano, April 2006, Proc IEEE Intl Symp on Biomedical Imaging ISBI. 2006. p. 698–701.

65. Neal RE, Rossmeisl JH, D'Alfonso V, Robertson JL, Garcia PA, Elankumaran S, et al. In vitro and numerical support for combinatorial irreversible electroporation and electrochemotherapy glioma treatment. Ann Biomed Eng. 2014;42(3):475–87. http://dx.doi.org/10.1007/s10439-013-0923-2
66. Rossmeisl JH, Garcia PA, Pancotto TE, Robertson JL, Henao-Guerrero, Neal RE, et al. Safety and feasibility of the NanoKnife system for irreversible electroporation ablative treatment of canine spontaneous intracranial gliomas. J Neurosurg. 2015;123(4):1008–25. http://dx.doi.org/10.3171/2014.12.JNS141768
67. Rossmeisl JH, Duncant RB, Huckle WR, Troy GC. Expression of vascular endothelial growth factor in tumors and plasma from dogs with primary intracranial neoplasms. Am J Vet Res. 68(11):1239–45. http://dx.doi.org/10.2460/ajvr.68.11.1239
68. Ellis TL, Garcia PA, Rossmeisl JH, Henao-Guerrero N, Robertson J, Davalos RV. Nonthermal irreversible electroporation for intracranial surgical applications. Laboratory investigation. J Neurosurg. 2011;114(3):681–8. http://dx.doi.org/10.3171/2010.5.JNS091448
69. Garcia PA, Pancotto T, Rossmeisl JH, Henao-Guerrero N, Gustafson NR, Daniel GB, et al. Non-thermal irreversible electroporation (N-TIRE) and adjuvant fractionated radiotherapeutic multimodal therapy for intracranial malignant glioma in a canine patient. Technol Cancer Res Treat. 2011;10(1):73–83. http://dx.doi.org/10.7785/tcrt.2012.500181
70. Duck F. Physical properties of tissues: A comprehensive reference book. San Diego, CA: Academic Press; 1990.
71. Cosman ER, Jr., Cosman ER, Sr. Electric and thermal field effects in tissue around. Am Acad Pain Med. 2005;6(6):405–24.